Biophysical Journal
Article

Biophysical Society

Flexural Rigidity and Shear Stiffness of Flagella Estimated from Induced Bends and Counterbends

Gang Xu,[1,*] Kate S. Wilson,[2] Ruth J. Okamoto,[2] Jin-Yu Shao,[3] Susan K. Dutcher,[4] and Philip V. Bayly[2]
[1]Department of Engineering and Physics, University of Central Oklahoma, Edmond, Oklahoma; [2]Department of Mechanical Engineering and Materials Science, [3]Department of Biomedical Engineering, and [4]Department of Genetics, Washington University in Saint Louis, Saint Louis, Missouri

ABSTRACT Motile cilia and flagella are whiplike cellular organelles that bend actively to propel cells or move fluid in passages such as airways, brain ventricles, and the oviduct. Efficient motile function of cilia and flagella depends on coordinated interactions between active forces from an array of motor proteins and passive mechanical resistance from the complex cytoskeletal structure (the axoneme). However, details of this coordination, including axonemal mechanics, remain unclear. We investigated two major mechanical parameters, flexural rigidity and interdoublet shear stiffness, of the flagellar axoneme in the unicellular alga *Chlamydomonas reinhardtii.* Combining experiment, theory, and finite element models, we demonstrate that the apparent flexural rigidity of the axoneme depends on both the intrinsic flexural rigidity (EI) and the elastic resistance to interdoublet sliding (shear stiffness, k_s). We estimated the average intrinsic flexural rigidity and interdoublet shear stiffness of wild-type *Chlamydomonas* flagella in vivo, rendered immotile by vanadate, to be $EI = 840 \pm 280$ pN$\cdot\mu$m^2 and $k_s = 79.6 \pm 10.5$ pN/rad, respectively. The corresponding values for the *pf3; cnk11-6* double mutant, which lacks the nexin-dynein regulatory complex (N-DRC), were $EI = 1011 \pm 183$ pN$\cdot\mu$m^2 and $k_s = 39.3 \pm 6.0$ pN/rad under the same conditions. Finally, in the *pf13A* mutant, which lacks outer dynein arms and inner dynein arm *c,* the estimates were $EI = 777 \pm 184$ pN$\cdot\mu$m^2 and $k_s = 43.3 \pm 7.7$ pN/rad. In the two mutant strains, the flexural rigidity is not significantly different from wild-type ($p > 0.05$), but the lack of N-DRC (in *pf3; cnk11-6*) or dynein arms (in *pf13A*) significantly reduces interdoublet shear stiffness. These differences may represent the contributions of the N-DRCs (~40 pN/rad) and residual dynein interactions (~35 pN/rad) to interdoublet sliding resistance in these immobilized *Chlamydomonas* flagella.

INTRODUCTION

Motile cilia and flagella are whiplike cellular organelles (~5–50 μm in length and ~200 nm in diameter) that bend actively to propel cells or move fluid or other materials (Fig. 1, *a* and *b*) (1). Motile cilia and flagella play a wide range of important roles in developmental and physiological processes, such as determination of left-right asymmetry, cerebrospinal fluid flow, mucociliary clearance, sperm swimming, and egg transport in fallopian tubes (1). Ciliary dysfunction is known or suspected in a number of genetic and acquired disorders (ciliopathies) including primary ciliary dyskinesia (2,3), chronic obstructive pulmonary disease (4), asthma (5), and otitis media (2). However, the complexity of the coupling between structure-function and mechanics-biochemistry in ciliary bending has precluded the mechanistic understanding required for rational development of diagnosis and treatment of ciliary dysfunction.

The ciliary microtubular cytoskeleton (axoneme) is a complex structure composed of >600 structural proteins (6). A typical axoneme (Fig. 1 *c*) consists of nine microtubule doublets that surround a central pair of singlet microtubules. These microtubule beams are interconnected by circumferential nexin-dynein regulatory complex (N-DRC) and radial spokes. In addition, motor protein dyneins form an array of cross bridges between neighboring outer doublets and exert forces (powered by ATP hydrolysis) that cause sliding of one doublet relative to the other (7). This interdoublet sliding is then converted to bending deformation of the axoneme as all microtubule beams are interconnected. The active motor forces are counterbalanced by both internal resistive forces from the axoneme and external viscous fluid drags (8). As a result, the axoneme undergoes coordinated propagation of bending deformations that are critical for motility.

Many details of this coordinated motion, including the role of axonemal mechanics, remain unclear. To date, only a

Submitted November 18, 2015, and accepted for publication May 10, 2016.
*Correspondence: gxu@uco.edu
Editor: Gijsje Koenderink.
http://dx.doi.org/10.1016/j.bpj.2016.05.017
© 2016 Biophysical Society.

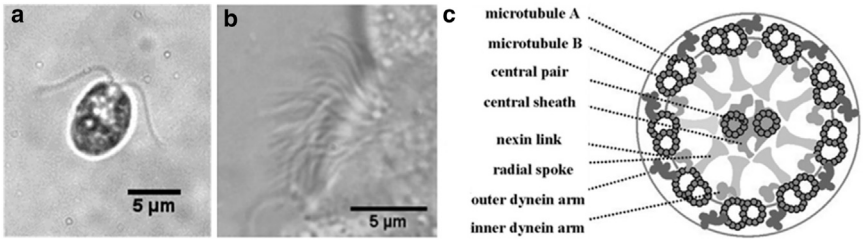

FIGURE 1 (*a* and *b*) Video micrographs of *Chlamydomonas* flagella (*a*) and human airway epithelial cilia (*b*). (*c*) Schematic of the normal flagellar axoneme in cross section (from Ibañez-Tallon et al. (1)). The "9+2" axoneme consists of nine outer microtubule doublets surrounding a central pair of single microtubules. These beam-like components are interconnected by radial spokes and nexin-dynein regulatory complexes (N-DRC). Interdoublet sliding is driven by dynein motor proteins.

limited number of studies directly measure the mechanical properties of the axoneme. Two mechanical parameters that are critical for characterizing the elastic behavior of the axoneme during bending are: 1) the flexural rigidity, *EI*, defined as the product of the Young's modulus, *E*, and the area moment of inertia, *I*; and 2) the interdoublet shear stiffness, k_s, defined as the elastic resistance to interdoublet sliding. In a previous study (9), the flexural rigidity of echinoderm sperm flagella, measured by bending with a flexible glass microneedle, was estimated to be in the range of $EI \sim 300–1500\ \text{pN}\cdot\mu\text{m}^2$. In sea urchin sperm studied with the same method, flexural rigidity was estimated to be $800\ \text{pN}\cdot\mu\text{m}^2$ (10). Using magnetic beads as mechanical probes, the flexural rigidity of human bronchial epithelial cilia was estimated to be $EI = \sim 620\ \text{pN}\cdot\mu\text{m}^2$ on average (11). Unlike a simple elastic beam, the axoneme is a complex bundle of interconnected microtubule doublets. The elastic resistance to interdoublet sliding, as well as the flexural rigidity, is needed to characterize its bending mechanics. The interdoublet shear stiffness of the axoneme is manifested through a characteristic phenomenon: the distal counterbend response to proximal bending (12–14). During large bending deformation, induced by a glass needle in the proximal portion of a sea urchin sperm flagellum, the distal portion of the flagellum exhibited a bend with the opposite curvature; this is referred to as the "counterbend" (13). By incorporating a shear-stiffness term in the classic elastic beam theory to analyze the counterbend curvature, the authors estimated both the intrinsic flexural rigidity ($EI = 100\ \text{pN}\cdot\mu\text{m}^2$) and shear stiffness ($k_s = \sim 6$ pN/rad) in sea urchin sperm flagella (13).

The ciliary axoneme is a highly conserved structure with similar protein composition and morphology between mammalian cilia and flagella of the unicellular alga, *Chlamydomonas reinhardtii* (15). Because of the considerable genetic and structural homology with human cilia, *Chlamydomonas* flagella have been used as a model system to investigate mechanisms of primary ciliary dyskinesia and other ciliopathies (16). The cumulative longitudinal shear forces on isolated *Chlamydomonas* axonemes have previously been measured (17); an effective cumulative spring constant was estimated to be ~2 pN/nm per 1 μm of axoneme (17), which for an effective diameter of 180 nm corresponds to $k_s = \sim 65$ pN/rad (13). However, the relationship between the bending compliance of the axoneme and its intrinsic flexural rigidity and interdoublet shear stiffness remains unclear, as do the contributions of the different structural components.

In this study, we combine experiment, theory, and modeling to investigate how the overall stiffness of *Chlamydomonas* flagella depends on both the flexural rigidity (attributable to microtubule doublets) and the interdoublet shear stiffness (from interconnecting components). The tip compliance of individual flagella was measured with the optical tweezers, while the interplay between bending and interdoublet shearing was probed by the counterbend induced by a microneedle. We estimated the average intrinsic flexural rigidity (*EI*) and interdoublet shear stiffness (k_s) in wild-type flagella, in the flagella of the *pf3;cnk11-6* mutant that lacks the N-DRC, has reduced tektin, and exhibits enhanced tubulin turnover at doublet tip (18–22), and in the flagella of *pf13A* mutants, which lack outer dynein arms and inner dynein arm *c* (23,24). We found that in both wild-type and mutant flagella the apparent flexural rigidity of the axoneme is greatly affected by elastic resistance to interdoublet sliding. Reductions in interdoublet shear stiffness, but not intrinsic flexural rigidity, were detected in both mutants using this approach, allowing us to estimate other contributions of N-DRC to shear stiffness.

MATERIALS AND METHODS

Cell culture and preparation

Wild-type (Strain CC-124), *pf3; cnk11-6* mutant (Strain CC-1026), and *pf13A* mutant (Strain CC-2492) cells were obtained from *Chlamydomonas* Resource Center at the University of Minnesota. Strain construction was performed using standard methods of mating and tetrad dissection (25). Genotypes were verified by PCR and sequencing of the mutations involved (26). In particular, the strain CC-1026 carries a second mutation (cnk11-6) in addition to the pf3 mutation (19) that results in longer flagella (19). *Chlamydomonas* cells were grown in modified Sager and Granick medium (25,27). All measurements were taken using nonbeating flagella with stable length. To suppress dynein activity (and beating), before all experiments, vanadate (Sigma, St. Louis, MO) was added to the medium, at a final concentration of 3 mM to block dynein activity (28). This concentration rendered all cells immotile within 5 min. The loss of motility was similar at higher concentrations of 4 and 5 mM; at 2 mM, cells remained motile for up to 10 min.

Measurement of tip compliance with optical tweezers

The tip compliance (ratio of displacement to force) of *Chlamydomonas* flagella was measured with an optical tweezers system (29). Briefly, an

optical trap and a micropipette controlled by a piezoelectric stage with nanometer resolution were positioned in an experimental chamber just above the objective of an inverted microscope (Fig. 2). Latex beads of 4.5 μm in diameter (Bangs Laboratories, Fishers, IN) were washed twice in PBS without Ca^{2+} and Mg^{2+} (Cambrex BioSciences, Walkersville, MD) containing 0.1% or 1% (w/v) BSA (bovine serum albumin; Fisher Scientific, Pittsburgh, PA) and mixed with the cells. Beads were coated with antibody targeted to flagellar membrane glycoproteins FMG-1 (30) to ensure frequent adhesion between the bead and the flagellum. A coated bead was trapped in an infrared laser focused by the objective. Trap stiffness was calibrated by applying controlled viscous drag forces to trapped beads, whose deflection was recorded and quantified with NanoTrack, a custom-written MatLab script (29). A cell was manipulated into the opening of the micropipette where it was firmly held by suction with one flagellum pointing upwards or downwards. The micropipette was driven toward the bead at 2.5 μm/s, paused for 0.1 s, then retracted at constant speed (Fig. 2, *a–c* and *a′–c′*). Bead deflection was tracked with NanoTrack; cell body displacement was calculated from the speed and duration of motion. The applied pulling force, F, was the product of the trap stiffness and bead deflection; the deflection of the flagellar tip, δ, was the difference between the displacements of the bead and cell body (Fig. 2 *d*). The tip compliance $C = \delta/F$.

Probing the interdoublet shear stiffness through the counterbend response

The effective shear stiffness of *Chlamydomonas* flagella was measured in a microprobe-based manipulation system. The cell body was firmly held by micropipette suction with one flagellum under microscope focus. A thin glass microneedle was driven by a 3D hydraulic micromanipulator (Narishige-US, East Meadow, NY) to approach and bend the flagellum at an intermediate length (Fig. 3, *a* and *b*). The flagellum reverses its curvature distal to the imposed bend beyond the forcing point; this is the counterbend response (Fig. 3 *b*). This behavior is consistent with a simple mechanical model in which doublets are interconnected by elastic elements. Sliding displacement between doublets will result in a local shear force that is proportional to the shear angle relative to the base, θ, modulated by the shear stiffness, k_s (in pN/rad). This effect is explained in the subsections below.

Data analysis: bending of beams with flexural rigidity and interdoublet shear stiffness

To estimate both the intrinsic flexural rigidity and the shear stiffness of the flagellum, we analyze data from both the tip compliance (optical tweezers)

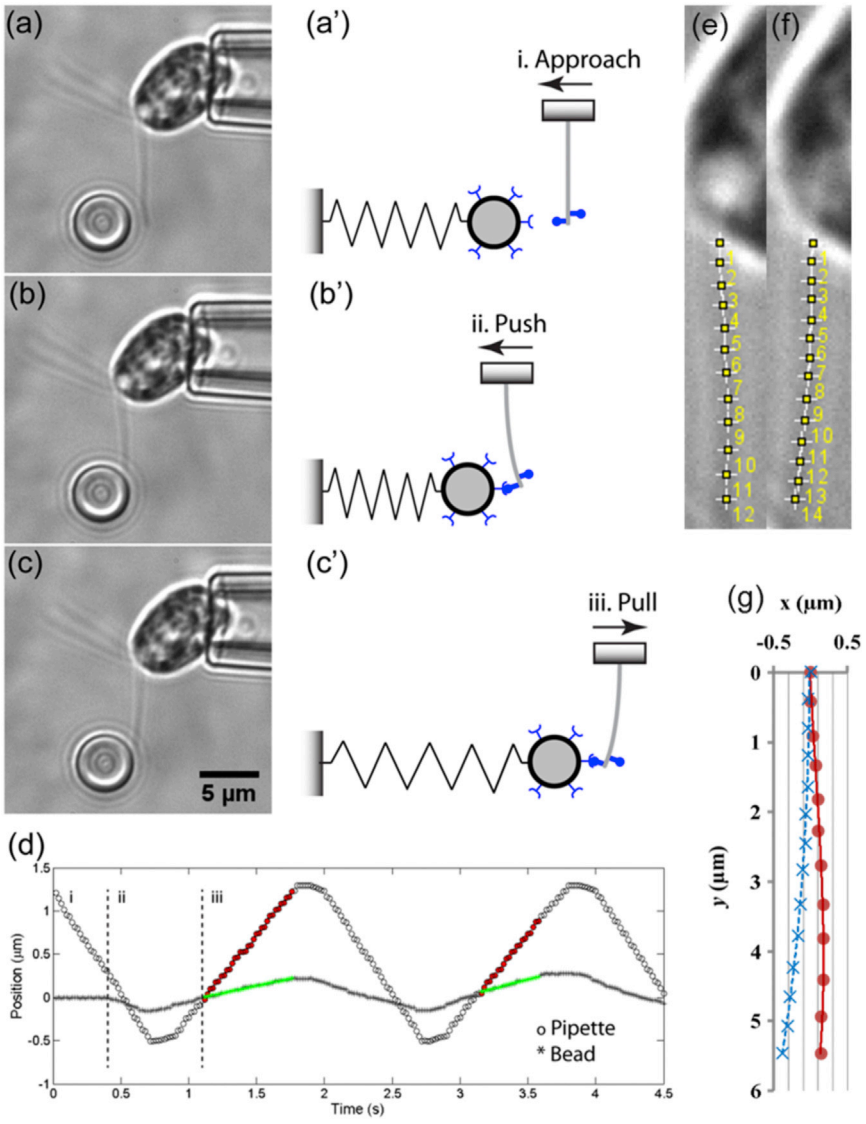

FIGURE 2 Measurement of the apparent flexural rigidity of the flagellar axoneme with optical tweezers. Video micrographs (*a–c*) and corresponding schematics (*a′–c′*) show the flagellum approaching, pushing, and pulling on a trapped bead. The trapped bead functions as a mechanical spring. The cell body was firmly held by micropipette suction and oriented such that force was applied perpendicularly to the flagellar axis. Adhesion between the bead and the flagellum was ensured by coating the bead with antibodies to FMG-1. (*d*) Typical tracking curves for relative pipette and bead positions (two pulling cycles are shown). Pulling forces on the flagellum were calculated from the product of the bead displacement (*green curve*) and the laser trap stiffness. Flagellar deflections were calculated from the difference between the displacements of the micropipette (*red curve*) and the bead (*green curve*). (*e* and *f*) Manual tracking of the flagellar length before (*e*) and after (*f*) bending in (*a*) and (*c*), respectively. (*g*) Superimposition of the tracked flagellar length in (*e*) and (*f*) showing that potential pivoting at the flagellar base is negligible compared with the induced bending close to the tip. To see this figure in color, go online.

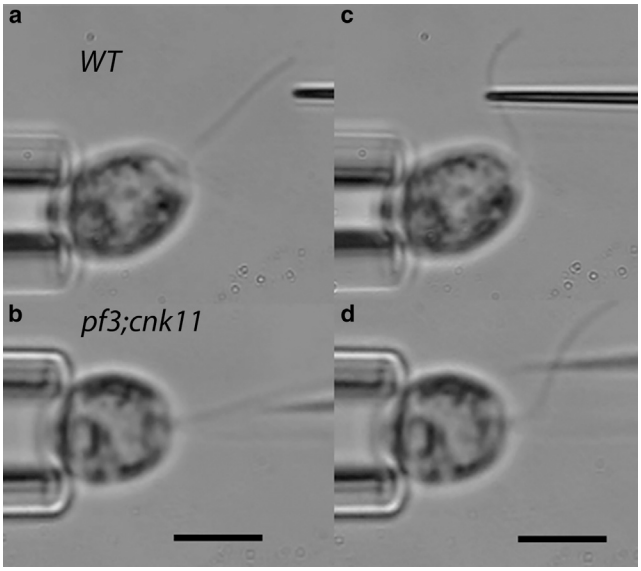

FIGURE 3 Estimation of the ratio of interdoublet shear stiffness to flexural rigidity from the counterbend response of the flagellar axoneme. Video micrographs show a flagellum (*a* and *b*) approached by, and (*c* and *d*) manipulated slowly with, a glass microprobe controlled by a hydraulic micromanipulator. The cell body was firmly held by micropipette suction. A bend of the flagellum is induced by the probe close to the base and is accompanied by a counterbend distal to the probe. Top row (*a* and *c*): wild-type (WT). Bottom row (*b* and *d*): *pf3; cnk11-6* double mutant. Scale bars, 5 μm.

and counterbend experiments in terms of the deflection of a slender beam with flexural rigidity EI (pN-μm^2) and resistance to shear deformation k_s (pN/rad), in response to point-loading at either the tip or near the midpoint (Fig. 4). The base is considered fixed (zero angular compliance). The fixed-base approximation is justified by consistent observations of negligible changes in the angle at the base during flagellar bending examples (e.g., see Fig. 3) in which large bending angles were observed distally.

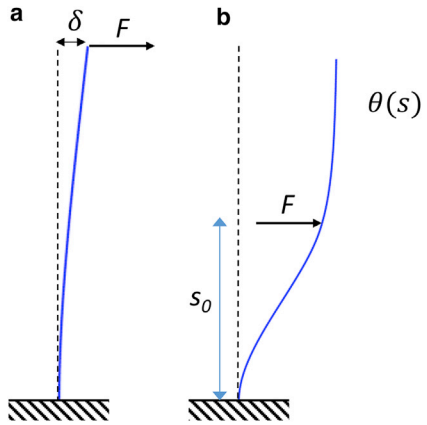

FIGURE 4 Mathematical models of the tip compliance and counterbend experiments. (*a*) A load, F, applied at the tip produces a deflection, δ. The tip compliance $C = \delta/F$ depends on both intrinsic flexural rigidity EI and shear stiffness k_s. (*b*) A load, F, applied near the midpoint (at $s = s_0$) produces a bend-counterbend shape described by the angle $\theta(s)$, which depends on the load amplitude, the location of the load, and on the ratio $\beta^2 = k_s/EI$. To see this figure in color, go online.

Analytical solution for flagellar deflection due to tip loading

The deflection, δ, at the tip of a fixed-free, slender (Euler-Bernoulli) beam with length L and flexural rigidity EI, but no shear stiffness, when a lateral force, F, is applied at the free end, is (31):

$$\delta = FL^3/3EI. \tag{1}$$

This theory must be extended to handle the flagellum, in which there is elastic resistance to shear. For quasi-static bending, equilibrium between moments from bending, shear resistance, and the external force must be maintained:

$$EI\frac{\partial^2\theta}{\partial s^2} - k_s\theta = -F. \tag{2}$$

A general solution to Eq. 2 is

$$\theta(s) = \frac{F}{k_s} + c_1 e^{\beta s} + c_2 e^{-\beta s}, \tag{3}$$

where $\beta = \sqrt{k_s/EI}$ (in μm^{-1}), and c_1 and c_2 are constants. The two boundary conditions are zero shear angle at the fixed base, $s = 0$:

$$\theta(0) = 0, \tag{4}$$

and zero moment (thus zero curvature) at the tip, $s = L$:

$$\left.\frac{\partial\theta}{\partial s}\right|_{s=L} = 0. \tag{5}$$

Using these two boundary conditions, we can solve for the two constants and obtain the solution for the shear angle

$$\theta(s) = \frac{F}{k_s}\left(1 - \frac{e^{\beta s}}{e^{2\beta L}+1} - \frac{e^{-\beta s}}{e^{-2\beta L}+1}\right). \tag{6}$$

Finally, the small deflection of the flagellar tip caused by the force is given by

$$\delta = \int_0^L \theta ds = \frac{FL}{k_s}\left(1 - \frac{1}{\beta L}\cdot\frac{e^{\beta L} - e^{-\beta L}}{e^{\beta L} + e^{-\beta L}}\right). \tag{7}$$

The tip compliance $C = \delta/F$ is thus:

$$C = \frac{L}{k_s}\left(1 - \frac{1}{\beta L}\cdot\frac{e^{\beta L} - e^{-\beta L}}{e^{\beta L} + e^{-\beta L}}\right). \tag{8}$$

The tip compliance depends on length, L, which is measured, as well as the shear stiffness, k_s, and the flexural rigidity, EI, both of which are unknown. Accordingly, counterbend experiments were performed to provide complementary information about the ratio $\beta^2 = k_s/EI$, as described in the next section.

Remark 1. The apparent flexural rigidity ($\overline{EI}$) of a beam with both flexural rigidity and shear stiffness can be calculated from the measured deflection (by analogy to Eq. 1) as:

$$\overline{EI} = \frac{FL^3}{3\delta}. \tag{9}$$

The ratio of apparent ($\overline{EI}$) to true flexural rigidity (EI), depends on both the parameter β and the length (L):

$$\frac{\overline{EI}}{EI} = \frac{\beta^3 L^3}{3\left(\beta L - \dfrac{e^{\beta L} - e^{-\beta L}}{e^{\beta L} + e^{-\beta L}}\right)}. \tag{10}$$

If $\beta L \ll 1$ (for very small shear stiffness), Eq. 10 predicts $\overline{EI} \approx EI$ as expected.

Remark 2. It can be shown (see Appendix A in the Supporting Material) that the apparent flexural rigidity $\overline{EI}$ should increase with length for a flagellum fixed at the base. A similar analysis can be performed for a flagellum loaded in "three-point bending", as in Okuno et al. (28). Importantly, the apparent flexural rigidity $\overline{EI}$ calculated from a three-point bending experiment will generally be different from (lower than) the corresponding value of $\overline{EI}$ calculated from the compliance of a tip-loaded, fixed-free flagellum with the same intrinsic properties (see Appendix A and Fig. A2 in the Supporting Material).

Analytical solution for flagellar shape in the counterbend experiment

An analytical solution for the shape of the counterbend has been presented recently in Gadêlha et al. (32); it is summarized here in terms of the current nomenclature. The equations of equilibrium (13) between bending and shearing that govern the quasi-static shape of the counterbend, in regions proximal and distal to the point of force application, respectively, are:

$$EI\frac{\partial^2\theta}{\partial s^2} - k_s\theta = -F, \quad s < s_0, \tag{11a}$$

$$EI\frac{\partial^2\theta}{\partial s^2} - k_s\theta = 0, \quad s \geq s_0, \tag{11b}$$

where EI is intrinsic flexural rigidity (without the overbar) attributable to the microtubule doublets and central pair.

A general solution to Eqs. 11a and 11b is

$$\theta(s) = \theta_1(s) = \frac{F}{k_s} + c_1 e^{\beta s} + c_2 e^{-\beta s}, \quad s < s_0; \tag{12a}$$

$$\theta(s) = \theta_2(\gamma) = d_1 e^{\beta\gamma} + d_2 e^{-\beta\gamma}, \quad s \geq s_0, \quad \gamma = s - s_0. \tag{12b}$$

Four boundary conditions are required to specify the shape of the flagellum. Two boundary conditions ensure zero angular deflection at the fixed end and zero moment at the free end of the flagellum:

$$BC_1 : \ \theta_1\big|_{s=0} = 0, \tag{13}$$

$$BC_2 : \ \left.\frac{\partial\theta}{\partial s}\right|_{s=L} = \left.\frac{\partial\theta_2}{\partial\gamma}\right|_{\gamma=\gamma_0} = 0, \quad (\gamma_0 = L - s_0). \tag{14}$$

The two remaining conditions ensure continuity of angle and curvature at the point of force application:

$$BC_3 : \ \theta_1\big|_{s=s_0} = \theta_2\big|_{\gamma=0}, \tag{15}$$

$$BC_4 : \ \left.\frac{\partial\theta_1}{\partial s}\right|_{s=s_0} = \left.\frac{\partial\theta_2}{\partial\gamma}\right|_{\gamma=0}. \tag{16}$$

These boundary conditions lead to algebraic equations that determine the four coefficients (c_1, c_2, d_1, d_2) for given values of F/k_s, β, and s_0 (see Appendix B in the Supporting Material).

Parameter estimation

First, the parameter β^2 was estimated from counterbend images by fitting the analytical solution (Eqs. 12a and 12b) to the observed flagellar shapes. Points on the flagellum were selected manually and fitted with a polynomial function for the shear angle, $\theta(s)$, in terms of the axial position, s (Fig. 5, *a* and *b*), using a previously developed algorithm (33). Numerical optimization (fminsearch; MATLAB, The MathWorks, Natick, MA) was used to find the ratio $\beta^2 = k_s/EI$ (13) and the value of s_0 that minimized the sum of the squared residual error between the analytical solution (Eqs. 12a and 12b) and the observed shear angle at 50 equally spaced points on the flagellum (Fig. 5, *c* and *d*). The fitting algorithm was validated on data from simulations of Eqs. 11a and 11b (COMSOL, Burlington MA; Fig. 5, *e–h*). Estimates were rejected if the squared error of the fitted solution exceeded 2% of the variance of the data, or if the optimized value of s_0 differed from the initial visual estimate s_0 by >10%. Each successful counterbend experiment produced a separate estimate of β^2, denoted $(\beta^2)^{(n)}$ ($n = 1, 2, \ldots, N$). For wild-type cells, $N = 12$ estimates of β^2 were obtained; for *pf3; cnk11-6*, $N = 8$, and for *pf13A*, $N = 11$.

Second, data from the tip compliance experiments, consisting of flagellar compliance (measured by optical tweezers) and length, were then used to estimate the physical parameters EI and k_s. In each mutant, the expression for the compliance of the flagellum as a function of length (Eq. 8) was fitted to data from all optical tweezers studies by minimizing the squared residual error between the predicted compliance (Eq. 8) and the data. Because different flagella were used in counterbend and tip compliance experiments, for each estimate $(\beta^2)^{(n)}$ ($n = 1, 2, \ldots, N$) from the counterbend experiments in a given mutant, a separate fit was performed to the ensemble of compliance data from that mutant (Fig. 6). Each such fit produced an independent estimate of $EI^{(n)}$, and a corresponding estimate of $k_s^{(n)} = (\beta^2)^{(n)} EI^{(n)}$.

Third and finally, statistical analysis of β^2, EI, and k_s estimates was performed using one-way ANOVA followed by multiple comparisons (Tukey-Kramer; MATLAB, The MathWorks). Normal distributions are assumed, and probability $p < 0.05$ was used as the threshold for statistical significance.

RESULTS

The counterbend response indicates shear resistance to interdoublet sliding

When bending was induced by a glass probe close to the base, each flagellum exhibited a counterbend distal to the probe (Figs. 3 and 5). Fitting Eqs. 12a and 12b to each flagellar shape provided an estimate of the ratio of the interdoublet shear stiffness to the intrinsic flexural rigidity (Fig. 6). For the wild-type flagella ($N = 12$), this ratio is $\beta^2 = 0.111 \pm 0.054\ \mu\text{m}^{-2}$; for the *pf3; cnk11-6* flagella ($N = 8$) $\beta^2 = 0.041 \pm 0.012\ \mu\text{m}^{-2}$; and for the *pf13A* flagella ($N = 11$), $\beta^2 = 0.061 \pm 0.028\ \mu\text{m}^{-2}$ (Fig. 6). Differences between wild-type and *pf3; cnk11-6* ($p = 0.0012$) and between wild-type and *pf13A* ($p = 0.0124$) are statistically significant.

Estimates of intrinsic flexural rigidity and interdoublet shear stiffness from tip compliance

We obtained estimates of EI and k_s in each flagella type by fitting Eq. 8 to all the measured values of compliance C from the optical tweezers experiments (Fig. 2), using each estimate of β^2 from the counterbend experiments in the corresponding flagella type (Fig. 6). The theoretical expression (Eq. 8) provides reasonably good fits (Fig. 7) to the compliance data for all values of β^2, supporting our postulate that

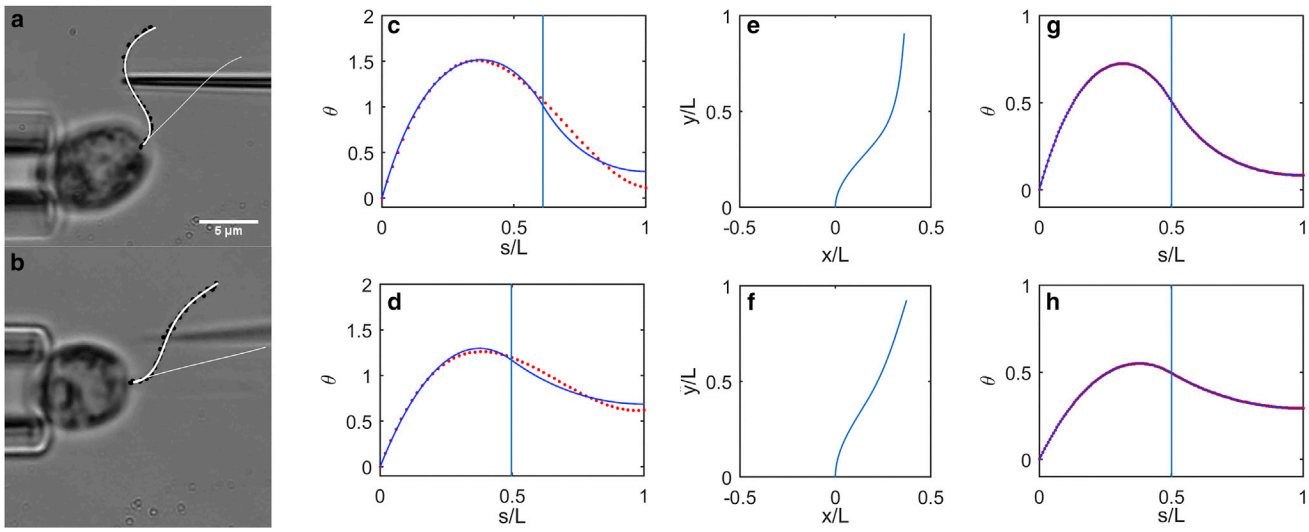

FIGURE 5 Examples of analytical solutions fitted to counterbend data from (*a–d*) experiment and (*e–h*) simulation. (*a*) Flagellum of wild-type *Chlamydomonas* (Fig. 3, *a* and *c*) with manually picked points (*black dots*) and a polynomial curve (*thick white line*) fitted to these points. The flagellum before bending is also shown (*thin white line*). (*b*) Flagellum of *pf3; cnk11-6 Chlamydomonas* (Fig. 3, *b* and *d*) with manually picked points (*black dots*) and a polynomial curve (*white*) fitted to these points. (*c*) Values of $\theta(s)$ (*red dots*) from polynomial curve fit in (*a*), and fitted solution (*blue curve*; Eqs. 12a and 12b) with $\beta^2 = 0.202$, $(\beta L)^2 = 25.5$. (*d*) Values of $\theta(s)$ (*red dots*) from a polynomial curve fit in (*b*), and a fitted solution (*blue curve*; Eqs. 12a and 12b) with $\beta^2 = 0.053$, $(\beta L)^2 = 5.0$. (*e*) Simulated shape of a beam with $(\beta L)^2 = 25$. (*f*) Simulated shape of a beam with $(\beta L)^2 = 5$. (*g*) Values of $\theta(s)$ at 50 equally spaced points on flagellum (*red dots*) from simulation with $(\beta L)^2 = 25$ and fitted solution (*blue curve*; Eqs. 12a and 12b). (*h*) Values of $\theta(s)$ (*red dots*) from simulation with $(\beta L)^2 = 5$ and fitted solution (*blue curve*; Eqs. 12a and 12b). To see this figure in color, go online.

the length-dependency of the compliance reflects both flexural rigidity and interdoublet shear stiffness. Statistical results are shown in Fig. 8.

The intrinsic flexural rigidity (attributed to the microtubule components) of the axoneme is estimated to be $EI = 840 \pm 280$ pN·μm^2 for wild-type flagella, $EI = 1011 \pm 183$ pN·μm^2 for the *pf3;cnk11-6* mutant, and $EI = 777 \pm 184$ pN·μm^2 for *pf13A* flagella, with no significant difference ($p > 0.05$) between any pair of groups (Fig. 8). On the other hand, the interdoublet shear stiffness of the axoneme differs markedly between these cell types: $k_s = 79.6 \pm 10.5$ pN/rad for the wild-type flagella, $k_s = 39.3 \pm 6.0$ pN/rad for the *pf3; cnk11-6* flagella, and $k_s = 43.3 \pm 7.7$ pN/rad for the *pf13A* flagella. Statistically significant differences ($p < 0.0001$) in k_s are observed between the wild-type flagella and each mutant (Fig. 8), but not between the two mutants. The reduction in shear stiffness in *pf3; cnk11-6* flagella is consistent with the loss of the circumferential linkages of N-DRC between doublets in this mutant. The reduction in shear stiffness in the *pf13A* mutant is consistent with a loss of shear resistance due to dynein arms that apparently contribute even though

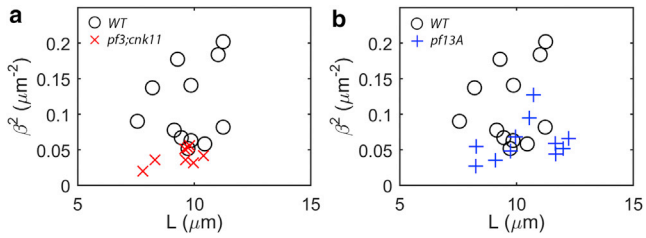

FIGURE 6 Analysis of the counterbend images yields the ratio of shear stiffness to flexural rigidity of the axoneme ($\beta^2 = k_s/EI$); individual estimates of β^2 are shown for (*a*) wild-type (WT) and *pf3; cnk11-6* flagella, and (*b*) WT and *pf13A* flagella. A statistically significant difference exists ($p = 0.0012$) between wild-type ($\beta^2 = 0.111 \pm 0.054$ μm^{-2}) and the *pf3; cnk11-6* mutant ($\beta^2 = 0.041 \pm 0.012$ μm^{-2}). The difference between WT and *pf13A* ($\beta^2 = 0.061 \pm 0.028$) is also statistically significant ($p = 0.012$). To see this figure in color, go online.

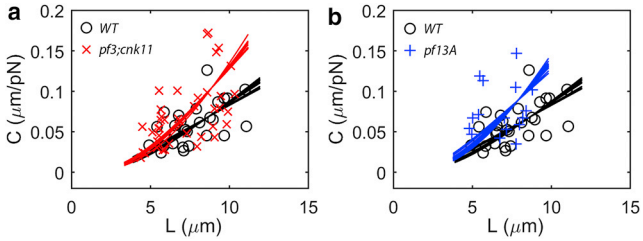

FIGURE 7 Flexural rigidity and shear stiffness are estimated from tip compliance and flagellar length by fitting the theoretical compliance-length relationship (Eq. 8) to data from the optical tweezers experiment. Each data point represents the tip compliance of an individual flagellum of either the (*a*) wild-type (WT) or *pf3; cnk11-6* mutant, or (*b*) WT or *pf13A* mutants. Each curve shows the theoretical compliance-length relationship (Eq. 8) for an estimate of β^2 from a specific counterbend experiment in the corresponding flagella type, using the value of k_s (or equivalently, EI) that minimizes the total squared residual error. The mean ($\pm$ SD) fraction of the variance explained by these curve fits is $R^2 = 0.89 \pm 0.01$ in wild-type ($N = 12$ curve fits), $R^2 = 0.76 \pm 0.01$ in *pf3; cnk11-6* ($N = 8$), and $R^2 = 0.79 \pm 0.01$ in *pf13A* ($N = 11$). To see this figure in color, go online.

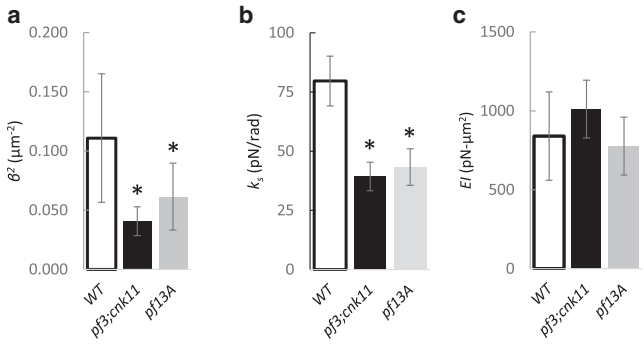

FIGURE 8 (*a–c*) Estimates of the intrinsic flexural rigidity and the shear stiffness of the axoneme obtained by fitting tip compliance data from optical tweezers studies to Eq. 8, using estimates of β^2 from each counterbend experiment. Asterisks denote statistically significant differences ($p < 0.05$, Tukey-Kramer multiple comparisons) compared to wild-type; *p*-values for the comparisons with wild-type are given below. The average intrinsic flexural rigidity and interdoublet shear stiffness of the wild-type axoneme are $EI = 840 \pm 280$ pN·μm^2 and $k_s = 79.6 \pm 10.5$ pN/rad, respectively. The corresponding values for the *pf3; cnk11-6* double mutant are $EI = 1011 \pm 183$ pN·μm^2 (NS, $p = 0.240$) and $k_s = 39.3 \pm 6.0$ pN/rad ($p < 0.0001$). The corresponding values for the *pf13A* mutant are $EI = 777 \pm 184$ pN·μm^2 (NS, $p = 0.785$) and $k_s = 43.3 \pm 7.7$ pN/rad ($p < 0.0001$).

the cells are in media containing high concentrations of vanadate.

We also estimated the apparent flexural rigidity (Eq. 10, Appendix A in the Supporting Material) of wild-type, *pf3; cnk11-6*, and *pf13A* flagella. The mean ($\pm$ SD) values of the apparent flexural rigidity were $\overline{EI} = 2978 \pm 1636$ pN·μm^2 ($L = 7.7 \pm 1.7$ μm) in wild-type flagella, 2155 ± 1389 pN·μm^2 ($L = 7.2 \pm 1.9$ μm) in *pf3; cnk11-6*, and 1733 ± 1121 pN·μm^2 ($L = 6.8 \pm 1.4$ μm) in *pf13A*. There was no statistically significant difference between any two groups. However, the apparent flexural rigidity showed a dependence on the flagellar length: the longer the flagellum, the larger the apparent flexural rigidity (Appendix A and Fig. A3 in the Supporting Material). This length-dependence of $\overline{EI}$ confirms the importance of shear stiffness (Appendix A and Fig. A2 in the Supporting Material). Performing two complementary measurements, such as tip compliance and counterbend, is necessary to estimate the intrinsic flexural rigidity.

DISCUSSION

The propulsive effectiveness of motile cilia and flagella relies on coordinated interactions between the mechanics and biochemistry of the axoneme. In this study, we probed two major mechanical parameters of the axoneme: the intrinsic flexural rigidity from the microtubules (outer doublets and central pair), and the interdoublet shear stiffness from interconnecting components. We developed a method, which, to our knowledge, is novel for determining the intrinsic mechanical properties of the axoneme, based on a combination of experiment and theory. Analytical expressions and finite element simulations (Appendix D and Fig. D2 in the Supporting Material) of a simplified structural model of the axoneme together demonstrate that the compliance, the apparent flexural rigidity, and the counterbend response of the axoneme all depend on the elastic resistance to interdoublet sliding.

We interpret the intrinsic flexural rigidity of the axoneme, *EI*, as due to the flexural rigidity of the beamlike components of the axoneme, presumably the outer microtubule doublets and the central pair. By analyzing experimental data based on our extended beam theory, we determined the average intrinsic flexural rigidity of the axoneme to be 840 ± 280 pN·μm^2 for the wild-type axoneme (Fig. 8), and not significantly different in the two mutants ($EI = 1011 \pm 183$ pN·μm^2 in *pf3; cnk11-6* flagella and $EI = 777 \pm 184$ in *pf13A*). These *EI* values are similar to a previous estimate of 900 pN·μm^2 for sea urchin sperm (28). For comparison, the flexural rigidity of individual microtubules was previously measured to be ~20–30 pN·μm^2 (34,35) (we note that other estimates are in the range of 5–8 pN·μm^2 (36,37)). Because the axoneme contains ~20 microtubules (18 combined into 9 outer doublets and 2 from the central pair), the combined overall flexural rigidity for the axoneme is at least 20 times of that for a single microtubule. If we accept the larger estimates of microtubule stiffness in the literature (34,35) the current estimates of intrinsic flexural rigidity (~800–1000 pN·μm^2) in *Chlamydomonas* flagella appear reasonable, considering that the bending stiffness of microtubule doublets should be larger than the sum of the bending stiffness from two individual microtubules (the area moment of inertia of the doublet is the sum of the area moments of inertia of two, almost-complete, microtubules relative to their own longitudinal axes, plus an additional amount due to the distance of the individual microtubule axes from the common parallel axis).

While the difference in *EI* between wild-type and *pf3; cnk11-6* flagella is not statistically significant, a small increase in the intrinsic flexural rigidity of *pf3; cnk11-6* flagella could reflect the effects of altered microtubule doublet ultrastructure. Axonemes of *pf3* mutants exhibit reduced levels of tektin, a filament protein that associates closely with tubulins in doublet microtubules (18–22). Microtubule doublets in the *cnk11* strain also exhibit altered tubulin dynamics (19) that mirror the effects of Taxol treatment (38).

The average interdoublet shear stiffness, k_s, was estimated to be $k_s = 79.6 \pm 10.5$ pN/rad for the wild-type flagellum, immobilized by vanadate in vivo. This shear stiffness includes the contributions of the N-DRC, as well as contributions of the radial spokes and any dynein arms that are not completely inactivated by vanadate. To estimate the contributions of individual components, we also measured k_s in flagella of *Chlamydomonas* mutants with specific axonemal defects. The interdoublet shear stiffness of *pf3; cnk11-6* flagella was $k_s = 39.3 \pm 6.0$ pN/rad

(Fig. 8), which is significantly less than that of the wild-type flagella ($p < 0.0001$). Previous studies have shown that the *pf3* and *pf3; cnk11-6* mutants lack the N-DRC. A plausible interpretation of our current results is that the contribution of the N-DRC to the shear stiffness is the difference between the k_s estimates in wild-type and *pf3; cnk11-6*:

$$k_s^{(\mathrm{NDRC})} = k_s^{(WT)} - k_s^{(pf3)} \approx 40 \text{ pN/rad}. \quad (17)$$

This estimate of $k_s^{(\mathrm{NDRC})}$ is larger than an estimate of ~6 pN/rad for demembranated sea urchin sperm axoneme obtained in a previous study (13). Notably, the counterbends observed in the prior study correspond to values of $\beta^2 = k_s/EI = 0.03$–$0.08\ \mu\mathrm{m}^{-2}$ (13), which are very similar to the values of β^2 found in this study. Thus this study and the prior study (13) agree with respect to the ratio of shear stiffness to flexural rigidity, but differ with respect to the total stiffness. In other previous work, Minoura et al. (17) measured the cumulative interdoublet longitudinal shear resistance, K_L, by applying longitudinal shear forces on isolated *Chlamydomonas* axonemes. This elastic constant was estimated by the authors to be $K_L = 2 \pm 0.8$ pN/nm per 1-μm section of the axoneme (17). To compare this to the current estimates of shear stiffness due to N-DRC (~40 pN/rad), we invoke Eq. D8 (see Appendix D in the Supporting Material) with $w = 180$ nm (following Pelle et al. (13)), and confirm that the data from Minoura et al. (17) are consistent with a value of $k_s = 65 \pm 26$ pN/rad.

Studies with the *pf13A* mutant address the contribution of residual dynein activity to the shear stiffness of flagella in the wild-type and *pf3;cnk11-6* mutant cells. Although a very high concentration of vanadate is present in the medium that contains the cells, and ATP is likely maintained at normal levels in the flagellum (~1.2 mM (39)), rendering flagella immotile, some dynein interactions with the microtubule doublets appear to remain and to resist shear. The difference (~35 pN/rad) between the k_s values in wild-type flagella and *pf13A* flagella is a plausible estimate of the stiffness provided by the outer and inner dynein arms that are missing in the *pf13A* mutant, but present in wild-type flagella. We note that the *pf13A* mutant retains inner dynein arms that may resist shear.

It is not clear why the interdoublet shear stiffness might differ between *Chlamydomonas* flagella and sea urchin sperm flagella, but differences in estimates of k_s might partly be due to structural differences in the two axonemes. For example, the N-DRC in *Chlamydomonas* has a bifurcated structure with two apparent interfaces with the B doublet microtubule, whereas one of the bifurcated heads of N-DRC from sea urchin sperm appears shorter and is possibly noninteracting (40). Thus the N-DRC in *Chlamydomonas* flagella may provide relatively more resistance to the interdoublet sliding than it does in sea urchin sperm. Also, although the overall structures of the radial spokes are similar between *Chlamydomonas* flagella and sea urchin sperm flagella (40), studies have shown that the radial spokes in *Chlamydomonas* flagella are structurally heterogeneous (41). Unlike flagella of other species with three regular radial spoke components (RS1, RS2, and RS3) that share the same structure, *Chlamydomonas* flagella have only two complete radial spoke components, RS1 and RS2, per axonemal repeat. The RS3S structure is structurally distinct in length, morphology, and anchoring to the microtubule doublets (41). In addition, radial spokes (RS1 and RS2) in *Chlamydomonas* flagella appear to be thicker and possess larger anchoring heads (Fig. 3, G and H, in Barber et al. (41)) than those in sea urchin sperm (Fig. 3 f in Nicastro et al. (42)). It seems counterintuitive that *Chlamydomonas* flagella, with fewer radial spokes, exhibit higher shear stiffness than sea urchin sperm flagella, but possible differences in interactions between N-DRCs and doublets may cause differences in resistance to interdoublet sliding. The possibility that true differences in flexural rigidity and interdoublet shear stiffness exist between different species warrants further study.

We note that the apparent flexural rigidity of *Chlamydomonas* flagella, $\overline{EI}$, as measured by optical tweezers, ranged from ~1000 to 4000 pN$\cdot\mu$m^2 for flagellar lengths from 4 to 10 μm (Appendix A and Fig. A3 in the Supporting Material). The magnitude of the apparent flexural rigidity is comparable to, but generally higher than, previous measurements on sperm flagella (9,10,13) and airway epithelial cilia (11), all of which fell in the range of 300–1500 pN$\cdot\mu$m^2. Some variations in measured values might result from structural differences among sperm flagella, mammalian cilia, and algal flagella (7,42–44). However, shear stiffness, flagellar length, loading, and boundary conditions all affect estimates of $\overline{EI}$ (Appendix SA). Our analysis confirms that when shear stiffness is significant, the apparent flexural rigidity of the flagellum, whether estimated by tip bending or three-point bending (28), depends on all these parameters (Appendix A and Fig. A2 in the Supporting Material). Thus measurements of bending stiffness or tip compliance should be complemented by independent measurements to assess the specific roles of flexural rigidity and shear stiffness.

CONCLUSIONS

In this study, we have developed an approach which, to our knowledge, is novel, combining two experimental protocols and corresponding theory, to quantify the intrinsic mechanical properties of the axoneme in *Chlamydomonas* flagella. These biophysical parameters are essential to investigations based on modeling and simulation (12,13,45). In particular, during ciliary beating, active dynein forces are balanced by both internal elastic forces within the axoneme and external viscous fluid drag (8,33). The intrinsic biomechanical properties are critical to accurate estimation of active forces generated by dynein motors (8). This study thus represents progress toward the long-term goal of quantitative

understanding of axonemal mechanics and function, which may ultimately lead to the development of novel diagnostic and therapeutic methods.

SUPPORTING MATERIAL

Supporting Materials and Methods and six figures are available at http://www.biophysj.org/biophysj/supplemental/S0006-3495(16)30299-5.

AUTHOR CONTRIBUTIONS

P.V.B., S.K.D., J.-Y.S., and G.X. designed research; G.X., K.S.W., and R.J.O. performed experiments and analyzed data; G.X. and P.V.B. developed the theory and model; and G.X., P.V.B., and S.K.D. wrote the article.

ACKNOWLEDGMENTS

We thank Dr. Bob Bloodgood (University of Virginia) for the antibody to FMG-1.

Funding from the Children's Discovery Institute, National Science Foundation grant No. CMMI-1265447 (to P.V.B.), National Institutes of Health grant No. NIGMS-032842 (to S.K.D.), and National Institutes of Health Institutional Development Award (IDeA) under grant No. 8P20GM103447 (to G.X.) is gratefully acknowledged.

REFERENCES

1. Ibañez-Tallon, I., N. Heintz, and H. Omran. 2003. To beat or not to beat: roles of cilia in development and disease. *Hum. Mol. Genet.* 12:R27–R35.
2. Ferkol, T., and M. Leigh. 2006. Primary ciliary dyskinesia and newborn respiratory distress. *Semin. Perinatol.* 30:335–340.
3. Leigh, M. W., J. E. Pittman, …, M. A. Zariwala. 2009. Clinical and genetic aspects of primary ciliary dyskinesia/Kartagener syndrome. *Genet. Med.* 11:473–487.
4. Wanner, A. 1990. The role of mucus in chronic obstructive pulmonary disease. *Chest.* 97:11S–15S.
5. Thomas, B., A. Rutman, …, C. O'Callaghan. 2010. Ciliary dysfunction and ultrastructural abnormalities are features of severe asthma. *J. Allergy Clin. Immunol.* 126:722–729.
6. Pazour, G. J., N. Agrin, …, G. B. Witman. 2005. Proteomic analysis of a eukaryotic cilium. *J. Cell Biol.* 170:103–113.
7. Nicastro, D., C. Schwartz, …, J. R. McIntosh. 2006. The molecular architecture of axonemes revealed by cryoelectron tomography. *Science.* 313:944–948.
8. Bayly, P. V., B. L. Lewis, …, S. K. Dutcher. 2011. Propulsive forces on the flagellum during locomotion of *Chlamydomonas reinhardtii*. *Biophys. J.* 100:2716–2725.
9. Okuno, M., and Y. Hiramoto. 1979. Direct measurements of the stiffness of echinoderm sperm flagella. *J. Exper. Biol.* 79:235–243.
10. Okuno, M., D. J. Asai, …, C. J. Brokaw. 1981. Effects of antibodies against dynein and tubulin on the stiffness of flagellar axonemes. *J. Cell Biol.* 91:689–694.
11. Hill, D. B., V. Swaminathan, …, R. Superfine. 2010. Force generation and dynamics of individual cilia under external loading. *Biophys. J.* 98:57–66.
12. Gadêlha, H., E. A. Gaffney, and A. Goriely. 2013. The counterbend phenomenon in flagellar axonemes and cross-linked filament bundles. *Proc. Natl. Acad. Sci. USA.* 110:12180–12185.
13. Pelle, D. W., C. J. Brokaw, …, C. B. Lindemann. 2009. Mechanical properties of the passive sea urchin sperm flagellum. *Cell Motil. Cytoskeleton.* 66:721–735.
14. Lindemann, C. B., L. J. Macauley, and K. A. Lesich. 2005. The counterbend phenomenon in dynein-disabled rat sperm flagella and what it reveals about the interdoublet elasticity. *Biophys. J.* 89:1165–1174.
15. Mitchell, D. R. 2000. *Chlamydomonas* flagella. *J. Phycol.* 36:261–273.
16. Lie, H., M. A. Zariwala, …, T. W. Ferkol. 2010. Primary ciliary dyskinesia in Amish communities. *J. Pediatr.* 156:1023–1025.
17. Minoura, I., T. Yagi, and R. Kamiya. 1999. Direct measurement of inter-doublet elasticity in flagellar axonemes. *Cell Struct. Funct.* 24:27–33.
18. Amos, L. A. 2008. The tektin family of microtubule-stabilizing proteins. *Genome Biol.* 9:229.
19. Lin, H., Z. Zhang, …, S. K. Dutcher. 2015. A NIMA-related kinase suppresses the flagellar instability associated with the loss of multiple axonemal structures. *PLoS Genet.* 11:e1005508.
20. Lin, J., D. Tritschler, …, D. Nicastro. 2011. Building blocks of the nexin-dynein regulatory complex in *Chlamydomonas* flagella. *J. Biol. Chem.* 286:29175–29191.
21. Linck, R., X. Fu, …, D. Nicastro. 2014. Insights into the structure and function of ciliary and flagellar doublet microtubules: tektins, Ca^{2+}-binding proteins, and stable protofilaments. *J. Biol. Chem.* 289:17427–17444.
22. Yanagisawa, H. A., and R. Kamiya. 2004. A tektin homologue is decreased in *Chlamydomonas* mutants lacking an axonemal inner-arm dynein. *Mol. Biol. Cell.* 15:2105–2115.
23. Huang, B., G. Piperno, and D. J. Luck. 1979. Paralyzed flagella mutants of *Chlamydomonas reinhardtii*. Defective for axonemal doublet microtubule arms. *J. Biol. Chem.* 254:3091–3099.
24. Omran, H., D. Kobayashi, …, H. Takeda. 2008. Ktu/PF13 is required for cytoplasmic pre-assembly of axonemal dyneins. *Nature.* 456:611–616.
25. Dutcher, S. K. 1995. Mating and tetrad analysis in *Chlamydomonas reinhardtii*. *Methods Cell Biol.* 47:531–540.
26. Dutcher, S. K., W. Gibbons, and W. B. Inwood. 1988. A genetic analysis of suppressors of the PF10 mutation in *Chlamydomonas reinhardtii*. *Genetics.* 120:965–976.
27. Dutcher, S. K. 1995. Flagellar assembly in two hundred and fifty easy-to-follow steps. *Trends Genet.* 11:398–404.
28. Okuno, M. 1980. Inhibition and relaxation of sea urchin sperm flagella by vanadate. *J. Cell Biol.* 85:712–725.
29. Xu, G., and J. Y. Shao. 2008. Human neutrophil surface protrusion under a point load: location independence and viscoelasticity. *Am. J. Physiol. Cell Physiol.* 295:C1434–C1444.
30. Bloodgood, R. A., M. P. Woodward, and N. L. Salomonsky. 1986. Redistribution and shedding of flagellar membrane glycoproteins visualized using an anti-carbohydrate monoclonal antibody and concanavalin A. *J. Cell Biol.* 102:1797–1812.
31. Byars, E. F., R. D. Snyder, and H. L. Plants. 1983. Engineering Mechanics of Deformable Bodies, 4th Ed. Harper & Row, New York.
32. Gadêlha, H., E. A. Gaffney, and A. Goriely. 2013. The counterbend phenomenon in flagellar axonemes and cross-linked filament bundles. *Proc. Natl. Acad. Sci. USA.* 110:12180–12185.
33. Bayly, P. V., B. L. Lewis, …, S. K. Dutcher. 2010. Efficient spatiotemporal analysis of the flagellar waveform of *Chlamydomonas reinhardtii*. *Cytoskeleton (Hoboken).* 67:56–69.
34. Mickey, B., and J. Howard. 1995. Rigidity of microtubules is increased by stabilizing agents. *J. Cell Biol.* 130:909–917.
35. Gittes, F., B. Mickey, …, J. Howard. 1993. Flexural rigidity of microtubules and actin filaments measured from thermal fluctuations in shape. *J. Cell Biol.* 120:923–934.

36. Felgner, H., R. Frank, and M. Schliwa. 1996. Flexural rigidity of microtubules measured with the use of optical tweezers. *J. Cell Sci.* 109:509–516.

37. Kikumoto, M., M. Kurachi, …, H. Tashiro. 2006. Flexural rigidity of individual microtubules measured by a buckling force with optical traps. *Biophys. J.* 90:1687–1696.

38. Schibler, M. J., and B. Huang. 1991. The colR4 and colR15 β-tubulin mutations in *Chlamydomonas reinhardtii* confer altered sensitivities to microtubule inhibitors and herbicides by enhancing microtubule stability. *J. Cell Biol.* 113:605–614.

39. Zhang, H., and D. R. Mitchell. 2004. Cpc1, a *Chlamydomonas* central pair protein with an adenylate kinase domain. *J. Cell Sci.* 117:4179–4188.

40. Pigino, G., A. Maheshwari, …, T. Ishikawa. 2012. Comparative structural analysis of eukaryotic flagella and cilia from *Chlamydomonas*, *Tetrahymena*, and sea urchins. *J. Struct. Biol.* 178:199–206.

41. Barber, C. F., T. Heuser, …, D. Nicastro. 2012. Three-dimensional structure of the radial spokes reveals heterogeneity and interactions with dyneins in *Chlamydomonas* flagella. *Mol. Biol. Cell.* 23:111–120.

42. Nicastro, D., J. R. McIntosh, and W. Baumeister. 2005. 3D structure of eukaryotic flagella in a quiescent state revealed by cryo-electron tomography. *Proc. Natl. Acad. Sci. USA.* 102:15889–15894.

43. Inaba, K. 2011. Sperm flagella: comparative and phylogenetic perspectives of protein components. *Mol. Human Reprod.* 17:524–538.

44. Satir, P., and S. T. Christensen. 2007. Overview of structure and function of mammalian cilia. *Annu. Rev. Physiol.* 69:377–400.

45. Cibert, C., J. Toscano, …, G. Bonnet. 2010. Bending of the "9+2" axoneme analyzed by the finite element method. *J. Theor. Biol.* 264:1089–1101.

Biophysical Journal, Volume *111*

Supplemental Information

Flexural Rigidity and Shear Stiffness of Flagella Estimated from Induced Bends and Counterbends

Gang Xu, Kate S. Wilson, Ruth J. Okamoto, Jin-Yu Shao, Susan K. Dutcher, and Philip V. Bayly

Appendix A. Apparent flexural rigidity of beams with both flexural rigidity and shear stiffness

We compare the apparent flexural rigidity of a beam with shear stiffness, simply supported and loaded at the midpoint (three-point bending), to the apparent flexural rigidity of the fixed-free beam (Eq. 10 in the main text). The equilibrium equations for beam with intrinsic flexural rigidity EI and shear resistance k_s in three-point bending with central load F (**Fig. A1**) are.

$$EI\frac{\partial^2\theta}{\partial s^2} - k_s\theta = -\frac{F}{2}. \qquad 0 < s < \frac{L}{2} \tag{A.1a}$$

$$EI\frac{\partial^2\theta}{\partial s^2} - k_s\theta = +\frac{F}{2}. \qquad \frac{L}{2} \le s < L \tag{A.1b}$$

Relevant boundary conditions for the beam are:

$$\left.\frac{\partial\theta}{\partial s}\right|_{s=0} = 0, \qquad \theta|_{s=L/2} = 0, \tag{A.2}$$

The solution for the tangent angle of the beam in the left half of the beam is:

$$\theta(s) = \frac{F}{2k_s}\left(1 - \frac{e^{\beta s} + e^{-\beta s}}{e^{\beta L/2} + e^{-\beta L/2}}\right), \qquad 0 < s < \frac{L}{2}. \tag{A.3}$$

where $\beta^2 = k_s/EI$.

The deflection at the midpoint in three-point bending in beam:

$$\delta = y(L/2) = \int_0^{L/2}\theta ds = \frac{FL}{4k_s}\left(1 - \frac{2}{\beta L}\cdot\frac{e^{\beta L/2} - e^{-\beta L/2}}{e^{\beta L/2} + e^{-\beta L/2}}\right). \tag{A.4}$$

For comparison, the deflection at the midpoint of an ideal Euler-Bernouilli beam with no shear resistance, in three-point bending is: $\delta_0 = \frac{FL^3}{48EI}$. Accordingly we define the apparent flexural rigidity of a beam with shear resistance, in three-point bending as: $\overline{EI} = \frac{FL^3}{48\delta}$. The ratio of apparent flexural rigidity to intrinsic flexural rigidity is thus.

$$\frac{\overline{EI}}{EI} = \frac{\delta_0}{\delta} = \frac{\beta^3L^3}{12\left(\beta L - 2\cdot\frac{e^{\beta L/2} - e^{-\beta L/2}}{e^{\beta L/2} + e^{-\beta L/2}}\right)} \tag{A.5}$$

As expected, this ratio approaches unity in the limit as $\beta L \to 0$, and increases with βL.

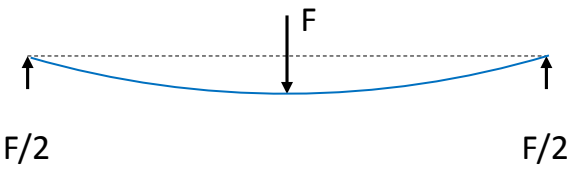

Figure A1. Free-body diagram of beam in three-point bending.

Comparing Eq. A.5 with Eq. 10 of this paper, we see that the apparent flexural rigidity of beams, for a given shear stiffness, increases with length in both loading scenarios, but at different rates. This can be seen in the graph of the non-dimensional ratio $\overline{EI}/EI$ vs the non-dimensional parameter βL (Fig. S2). The dimensional value of apparent flexural rigidity , $\overline{EI}$, is plotted vs length for representative parameter values, for both three-point bending of a simply-supported beam and tip loading of a fixed-free beam. It is clear that the two measurement protocols give very different estimates of $\overline{EI}$, and that the estimates diverge as length increases.

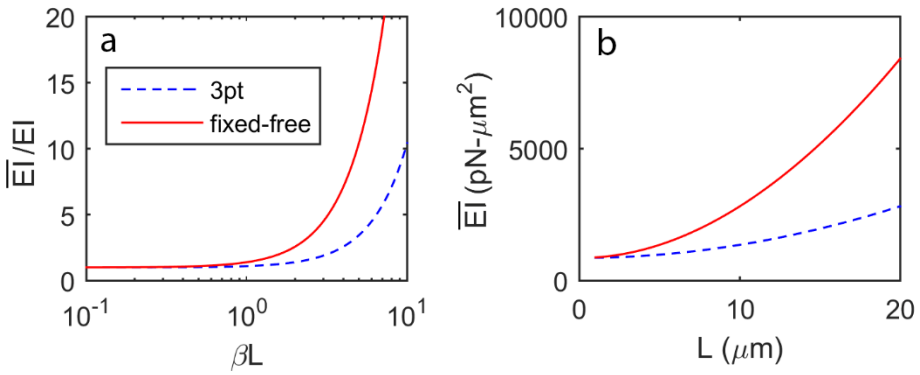

Figure A2. (a) Non-dimensional ratio of apparent flexural rigidity $\overline{EI}$ to intrinsic flexural rigidity EI for beams under different test conditions, as a function of the non-dimensional parameter βL. (b) Apparent (dimensional) flexural rigidity $\overline{EI}$ of a beam with intrinsic flexural rigidity $EI = 860\ \mathrm{pN \cdot \mu m^2}$ and shear stiffness $k_s = 50\ \mathrm{pN/rad}$, under different test conditions. Solid red curves: $\overline{EI}$ estimated from the deflection of a fix-free beam loaded at the tip. Dashed blue curves: $\overline{EI}$ estimated from the deflection at the mid-point of a simply-supported beam loaded at its midpoint (three-point bending).

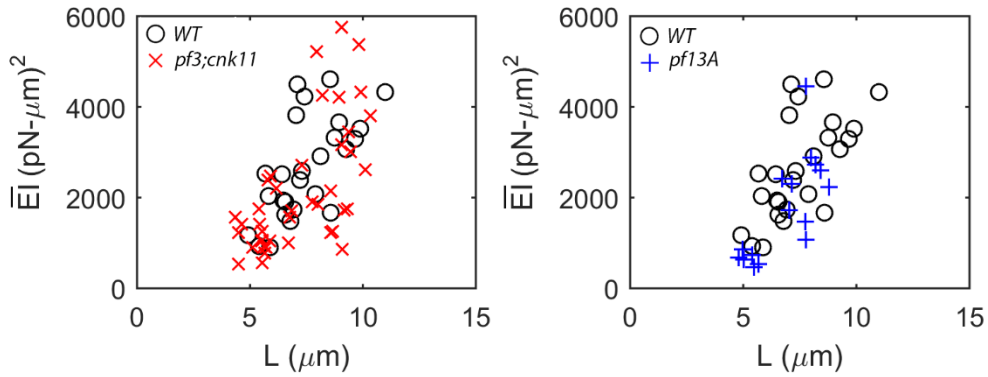

Figure A3. Apparent flexural rigidity $\overline{EI}$ of flagella measured by optical trap technique in wild-type *Chlamydomonas*, and in *pf3; cnk11-6* and *pf13A* mutants.

Appendix B. Details of the closed form solution for the counterbend experiment

The analytical solution for the shape of a beam subjected to a perpendicular point load at s_0 is given by Eqs. (12-16) from the main text:

$$\theta(s) = \theta_1(s) = \frac{F}{k_s} + c_1 e^{\beta s} + c_2 e^{-\beta s}, \qquad s < s_0, \tag{12a}$$

$$\theta(s) = \theta_2(\gamma) = d_1 e^{\beta \gamma} + d_2 e^{-\beta \gamma}, \qquad s \geq s_0, \quad \gamma = s - s_0. \tag{12b}$$

The four boundary conditions (Eqs. 13-16 in the paper) are also repeated here:

$$BC_1: \quad \theta_1|_{s=0} = 0, \tag{13}$$

$$BC_2: \quad \left.\frac{\partial \theta}{\partial s}\right|_{s=L} = \left.\frac{\partial \theta_2}{\partial \gamma}\right|_{\gamma=\gamma_0} = 0, \quad (\gamma_0 = L - s_0) \tag{14}$$

$$BC_3: \quad \theta_1|_{s=s_0} = \theta_2|_{\gamma=0}, \tag{15}$$

$$BC_4: \quad \left.\frac{\partial \theta_1}{\partial s}\right|_{s=s_0} = \left.\frac{\partial \theta_2}{\partial \gamma}\right|_{\gamma=0} \tag{16}$$

These boundary conditions lead to algebraic equations which determine the four coefficients (c_1, c_2, d_1, d_2) for given values of F, k_s (or EI), β, L, and s_0.

$$BC_1: \quad \frac{F}{k_s} + c_1 + c_2 = 0, \tag{B.1}$$

$$BC_2: \quad \beta\left(d_1 e^{\beta \gamma_0} - d_2 e^{-\beta \gamma_0}\right) = 0, \tag{B.2}$$

$$BC_3: \quad \frac{F}{k_s} + c_1 e^{\beta s_0} + c_2 e^{-\beta s_0} = d_1 + d_2, \tag{B.3}$$

$$BC_4: \quad \beta\left(c_1 e^{\beta s_0} - c_2 e^{-\beta s_0}\right) = \beta(d_1 - d_2). \tag{B.4}$$

where $\gamma_0 = L - s_0$ (the length of the section distal to the point load).

These equations may be solved simultaneously to give the coefficients

$$c_2 = \frac{\frac{F}{k_s}\left(\frac{1 - e^{-\beta s_0}}{e^{\beta s_0} - e^{-\beta s_0}} - \frac{e^{-\beta s_0}}{e^{\beta s_0} + e^{-\beta s_0}}\right)}{\left(\frac{1 + e^{2\beta \gamma_0}}{e^{\beta s_0} - e^{-\beta s_0}} - \frac{1 - e^{2\beta \gamma_0}}{e^{\beta s_0} + e^{-\beta s_0}}\right)} \tag{B.5}$$

$$c_1 = c_2\left(\frac{1 - e^{2\beta \gamma_0}}{e^{\beta s_0} + e^{-\beta s_0}}\right) - \frac{\left(\frac{F}{k_s}\right) e^{-\beta s_0}}{e^{\beta s_0} + e^{-\beta s_0}} \tag{B.6}$$

$$d_1 = -c_1 - \frac{F}{k_s} \tag{B.7}$$

$$d_2 = c_2 e^{2\beta \gamma_0} \tag{B.8}$$

Appendix C. General relationships between tip compliance and flagellar length

If the tip deflection in response to a point load were solely due to simple bending (as in an Euler-Bernouilli beam with flexural rigidity EI) the tip compliance would be:

$$C = \frac{\delta}{F} = \frac{L^3}{3EI} \qquad (C.1)$$

If the tip deflection were solely due to rotation at the base, subject to the restoring force of a spring with torsional stiffness k_B $(\mathrm{pN \cdot \mu m/rad})$ the tip compliance would be:

$$C = \frac{\delta}{F} = \frac{L^2}{k_B} \qquad (C.2)$$

If the tip deflection were solely due to shear deformation, resisted by shear stiffness k_s $(\mathrm{pN/rad})$ the tip compliance would be:

$$C = \frac{\delta}{F} = \frac{L}{k_s} \qquad (C.3)$$

For the first case (pure bending) the log-log plot of compliance vs. length would have a slope of 3, in the second case (pure base rotation) the log-log plot would have a slope of 2, and in the third case the log-log plot would have a slope of 1.

Figure C1 shows the raw compliance measurements for wild-type, *pf3; cnk11-6,* and *pf13A* mutants plotted on log-log scales. Also shown are simple linear fits to the log-log data.

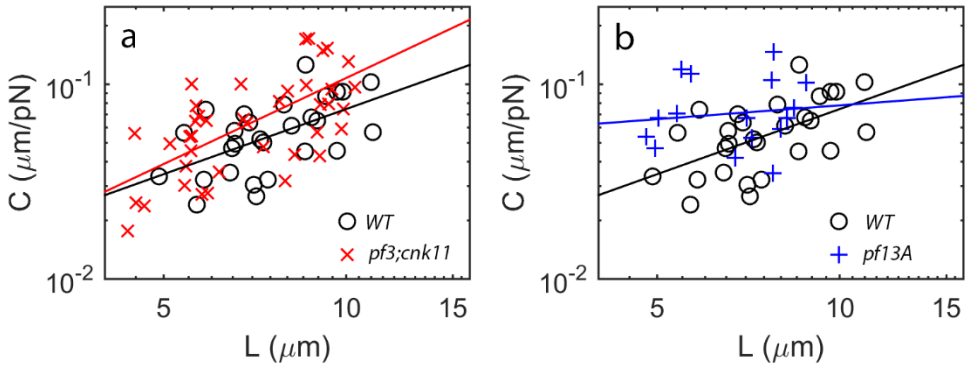

Figure C1. Log-log plots of tip compliance vs flagellar length in Chlamydomonas flagella, measured using optical tweezers. The slopes of the best-fit lines to the log-log data are 1.11 (wild-type), 1.47 (*pf3; cnk11-6*) and 0.24 (*pf13A*).

The slopes of the log-log plots of compliance vs length are all much less than 3. Since counterbend experiments confirm minimal rotation at the base, it is likely that shear stiffness plays an important role in determining the tip compliance. The very low slope of the compliance-length relationship in the *pf13A* mutant suggests unmodeled physical characteristics, such as a non-uniform longitudinal distribution of shear stiffness.

Appendix D. Structural finite element models of flagellar bending

To directly examine the effect of inter-doublet sliding resistance on the overall apparent flexural rigidity and the counterbend response of the axoneme, nonlinear 2D finite-element computational models for the axoneme were created, using the finite-element software ABAQUS (v.6.7, Abaqus, Inc., Providence, RI). Utilizing built-in mechanical elements in the software, the microtubule doublets were represented by two elastic beams (10 μm long and 240 nm separation) and all interconnecting structures (nexin links, radial spokes, e.g.) by an array of 100 trusses (to control spacing) and 100 springs (to resist sliding) (Fig. D1). Despite its simplicity, this axoneme model recapitulates the overall structural and mechanical properties of the axoneme. The intrinsic flexural rigidity (EI pN·μm2) was provided by two beam elements each with flexural rigidity $EI/2$, while the values of the elastic constant, k_k, for the springs were varied over a wide range.

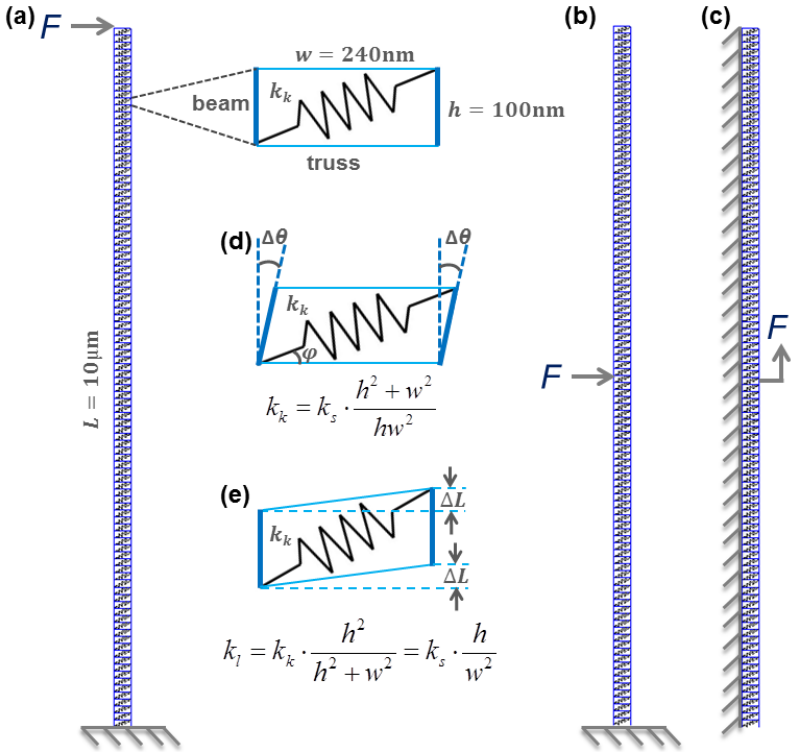

Figure D1. The 2D finite element model of the axoneme. The axoneme is modeled as two 10-μm-long elastic beams cross-linked by an array of 100 truss elements (to maintain spacing) and 100 springs (to resist sliding, inset in a). (a) A concentrated force is applied perpendicular to the beam at the tip of the beam, to cause a slight bending deformation (in analogy to the optical tweezers experiment). (b) A concentrated force is applied perpendicular to the beam at the mid-point to bend the proximal half of the beam (as in the counterbend experiment). Models in (a) and (b) were used to study how the apparent flexural rigidity and the counterbend response of the beam depend on the inter-beam shear stiffness provided by the interconnecting springs. (c) A concentrated force along the longitudinal axis of the beam is applied at the mid-point to cause a small shear displacement of one beam relative to the other, as in Minoura et al [1]. (d) For small deflections, the elasticity of the springs, k_k, is directly related to the shear stiffness, k_s, through Eq. D.3. (e) For small inter-beam sliding displacements, the total longitudinal stiffness, K_L, is directly related to the shear stiffness, k_s, through Eq. D.8.

To simulate the tip compliance test, a small point force was applied at the tip of the beam assembly (Fig. D1a) and the resulting tip deflection was recorded. The apparent flexural rigidity of the beam was also determined using Eq. 10 of this paper. To simulate the counterbend experiment, a point force was applied to the midpoint of the flagellum (Fig. D1b) to induce a large bend in the proximal section, and the response of distal portion of the beam was examined. To simulate longitudinal shear testing on the isolated axoneme (as in Minoura et al. [1]), we fixed one of the two beams and applied a small concentrated force along the length of the other beam (Fig. D1c). Division of the applied force by the resulting longitudinal displacement of the beam yields a cumulative longitudinal stiffness, K_L, that resists inter-doublet sliding.

Due to the simplicity of our structural model for the axoneme, both the individual spring and longitudinal elastic constants can be expressed in terms of the shear stiffness, k_s. First, consider a unit cell during a small bending deformation accompanied by a small angular displacement, $\Delta\theta \ll 1$ (Fig. D1d), then the extension of the spring is given by

$$\Delta l_k = l - l_0 = \sqrt{(w + h\sin\Delta\theta)^2 + (h\cos\Delta\theta)^2} - \sqrt{w^2 + h^2} \approx \frac{hw\Delta\theta}{\sqrt{w^2 + h^2}}. \qquad (D.1)$$

The perpendicular component of the resulting spring force can be determined and also related to the shear stiffness, k_s , as

$$F_{k_\perp} = k_k \Delta l_k \cos\varphi = k_s \Delta\theta. \qquad (D.2)$$

Using $\cos\varphi = w/\sqrt{w^2 + h^2}$, the spring stiffness can be related to shear stiffness, k_s:

$$k_k = k_s \cdot \frac{h^2 + w^2}{hw^2}. \qquad (D.3)$$

Next, consider a unit cell from the model with one of the two beams having a small relative displacement, ΔL, along the longitudinal direction (Fig. D1e), then the corresponding extension of the spring is given by

$$\Delta l_k = l - l_0 = \sqrt{w^2 + (h + \Delta L)^2} - \sqrt{w^2 + h^2} \approx \frac{h\Delta L}{\sqrt{w^2 + h^2}}. \qquad (D.4)$$

Thus, the longitudinal (along the beam length) component of the resulting spring force can be determined and also related to the longitudinal stiffness as

$$F_{k_\parallel} = k_k \Delta l_k \sin\varphi = k_l \Delta L. \qquad (D.5)$$

Using $\sin\varphi = h/\sqrt{w^2 + h^2}$, we can write:

$$k_l = k_k \cdot \frac{h^2}{h^2 + w^2}. \qquad (D.6)$$

Finally, combining Eqs. 19 and 22, we can express the longitudinal stiffness in terms of the shear stiffness

$$k_l = k_s \cdot \frac{h}{w^2}. \qquad (D.7)$$

Both the spring element stiffness k_k and the resulting longitudinal shear stiffness k_l of each spring element both have units of pN/nm. The cumulative longitudinal stiffness, $K_L = k_l N$, where $N = L/h$ is the number of spring elements (100 in our models). In terms of k_s:

$$K_L = k_s \cdot \frac{L}{w^2} \qquad (D.8)$$

We used the simplified 2D finite element computational model above to simulate the tip-bending and counterbend experiments. This model confirms that the apparent flexural rigidity depends on the shear stiffness (Appendix A). When the shear stiffness (as implemented through the elastic constant of the interconnecting springs) is relatively small, there are negligible connections between the two component beams so each individual beam can bend along its own neutral axis. As a result, the apparent flexural rigidity is simply the same as the combined intrinsic flexural rigidity from the two component beams, or $\overline{EI}/EI = 1$ (Fig. D2a). The apparent flexural rigidity increases with increasing shear stiffness until it reaches a plateau for very high spring stiffness (Fig. D2a). The plateau value for the apparent flexural rigidity with very high spring stiffness (higher than the tensile stiffness of the doublets) can be predicted by the parallel axis theorem; the two component beams would extend and compress due to bending along a neutral axis centered between them.

The finite element model also shows that magnitude of the shear stiffness determines the behavior of the distal portion of the flagellum when the proximal region is bent by a concentrated force (Fig. D2b). Small shear stiffness provides little resistance to sliding, and the distal portion of the complex beam remains straight and rotates with the base (Fig. D2b-left panel). For large shear stiffness, there is a sharp, local bend near the point of loading, and the distal portion of the complex beam remains relatively straight (Fig. D2b-right panel). It is only when the shear stiffness is intermediate that the complex beam exhibits a clear counterbend (Fig. D2b-middle panel), like those observed in our experiments.

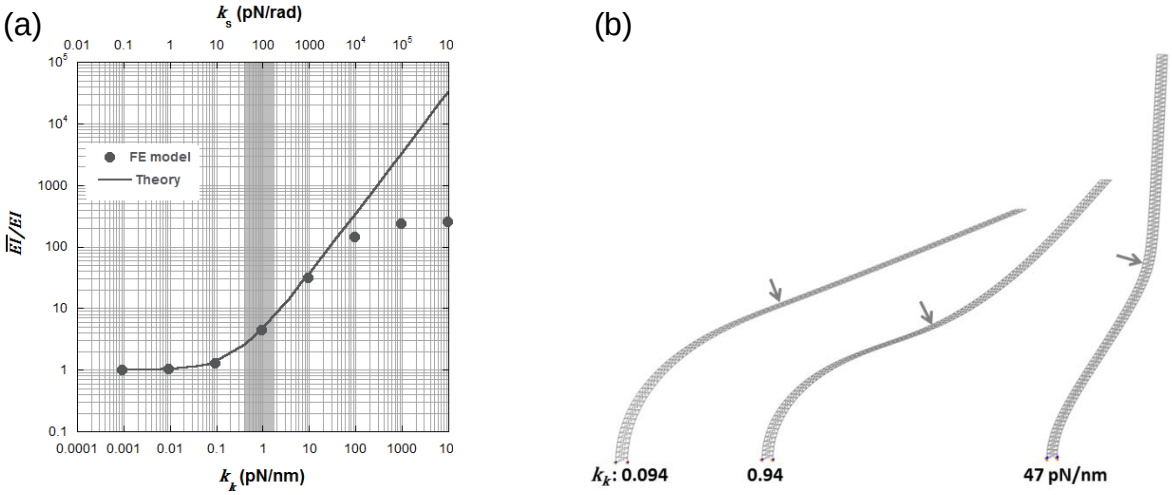

Figure D2. Results from a finite element model of the axoneme show that the tip compliance, apparent flexural rigidity, and counterbend response of the axoneme strongly depend on the inter-doublet shear stiffness, k_S, which depends in turn on the stiffness of connecting springs, k_k (Eq. D.3). (a) The apparent flexural rigidity increases with increasing spring stiffness. When the spring stiffness, k_k, is very small, the apparent flexural rigidity is about the same as the simple sum of the flexural rigidities of the component beams. When the spring stiffness k_k is too large to allow any inter-beam sliding, the apparent flexural rigidity of the whole structure reaches a plateau that can be predicted by the parallel-axis theorem. The shaded region of the data corresponds to the intermediate shear stiffness values estimated from experimental studies of wild-type flagella. Also shown is theoretical curve for the ratio based on Eq. 10 of this paper. (b) When the proximal half of the axoneme model is bent by a concentrated force applied at the mid-point, only the beam with the intermediate shear stiffness (k_k=0.94 pN/nm estimated from the experimental value of k_S=80 pN/rad for wild-type flagella) exhibits a clear counterbend response. From left to right: small, intermediate, and large shear stiffness, respectively.

REFERENCES

[1] I. Minoura, T. Yagi, and R. Kamiya, "Direct measurement of inter-doublet elasticity in flagellar axonemes," *Cell Struct Funct,* vol. 24, pp. 27-33, Feb 1999.